Calcium Hydroxylapatite Stone's Organic Zinc Dependency

Nicholas Jaber, Vincent Blay, Misun Khang, Sunita Ho

Abstract

Although many have theorized how calcium hydroxylapatite, salivary, kidney and prostate, stones mineralize in a similar manner to that of bone. Analysis of the mechanism for how the mineralization process is similar has not been tested. We studied the relation between a moving average of autofluorescence and x-ray fluorescence zinc expression. We have found a positive relation between autofluorescence and x-ray fluorescence zinc expression. By comparing moving averages of zinc, autofluorescence dependence we state that calcium hydroxylapatite stone's zinc is likely originating from an organic substrate.

Introduction

Mineralization is the process by which organic matter is completely converted to its inorganic constituents by microbes.[1] ''Biomineralization is the chemical alteration of an environment by microbial activity that results in the precipitation of minerals".[2] Pathologic mineralization is the disease by which microbes cause the formation of anomalous minerals. These minerals take two anomalous forms: those that are extraskeletal, and those that are of an atypical composition. In this paper, we will be comparing extraskeletal pathologic biominerals. Biominerals which are mislocated are classified into two different categories: stones and plaques. In this paper we will be investigating mineralized stones. Biominerals can form as one of many common mineral types. The biominerals ordered by prevalence in salivary stones are: calcium hydroxylapatite, whitlockite, octacalciumphosphate, and brushite.[3] Biominerals ordered by prevalence in kidney stones are: oxalate, calcium hydroxylapatite, struvite, uric acid, cystine stones and medication related stones.[4–6] Biominerals ordered by prevalence in prostate stones are: calcium

hydroxylapatite, whitlockite and calcite.[7] Of these mineral types calcium hydroxylapatite is the only common mineral in each of these stone types. These minerals form most readily in 7.4 pH conditions.[8,9] This paper will be comparing pathologic calcium hydroxyl-apatite (PCHA) stones in the secretory and excretory systems of humans. PCHA stones form in salivary glands, kidneys, and prostate glands.

Looking into the anatomy of these three glands we find that. Of the three salivary glands, the submandibular gland accounts for ~80% of salivary stone formations.[10] This is generally accepted to be as a result of mixing between serous and mucous saliva. The nodules where the saliva is produced are connected by a branching network of ducts until they empty into the mouth as one duct. Stones most often form in this branching network of ducts. In the kidney there are 8-12 papilla, which each consist of hundreds of thousands of nephrons which filter blood and dispense lumen into larger collecting ducts. These collecting ducts then output into the calyx of the kidney. There is still some debate about where within the kidney these stones form, but these stones are typically extracted from the calyx of the kidney. Prostate stones are found in the ducts of the prostate and are often found even in healthy men. These stones are only removed when many of these stones cause significant stricture.

The nanostructure of these PCHA stones are formulated of heterogeneous mixtures of nanoparticles. One of these nanoparticle types is a spherical mineralized nanoparticle which has been documented as: calcified nanoparticles (CNP), nanoparticles (NP), radial crystallites. All of these names are in reference to the same observed characteristics, and all make assumptions about the nature of the mineral formation process. The term CNP makes assumptions about the mineral being calcified, and the other terms are not specific enough to differentiate between different nanoparticles present in these heterogeneous PCHA stones. That is why we decided to

introduce new terminology to the related lexicon. As the name suggests, spherical mineralized nanoparticles are minerals that form in a spherical shape possibly due to the thermodynamic stability associated with spherical mineral formation described in Ostwald's ripening theory.[11] These CNP structures are often found during the early stages of bone development on the zinc rich growth plates of children. Zinc has been correlated to promoting bone development. Zinc serves many purposes throughout the body, but zinc is predominantly found in a catalytic, cocatalytic or structural capacity.[12,13] These cocatalytic zinc functional groups are commonly found in bone development interfaces.[14,15] Zinc presence is decreased in association with aging, skeletal unloading, and postmenopausal conditions.[14,16] As a result, zinc content in bone has been used as an indicator for overall bone health.[16]

With a comprehensive understanding of the above topics one can piece together the current thought in the field of PCHA stone development. Although there have been many proposed mechanisms as to how PCHA stones form, a clear understanding of how the mineralization cascade is initiated remains elusive. Many groups have studied zinc, mineral density relationship, and theorized the similarities between bone development and PCHA stone development. In this study we attempt to test the validity of this theory by using correlative image processing to identify co-localizations between zinc and amino acids, as well as co-localizing mineralization order and zinc. Co-localizing zinc and amino acids would validate that the zinc is coming from an organic substrate. Colocalization between low order (under-developed) CNPs and mineral density would appear to indicate that zinc may be serving as either a catalytic function similar to the development of bone, or as an inhibitor of CNP development. With the addition of molecular analysis we can identify if the presence of the zinc serves as an inhibitor or as a catalytic function in the reaction between calcium carbonate and

phosphate. All of this should provide evidence to confirm or deny the theoretical model that PCHA stone development is similar to that of bone development.

Materials and Methods

Sample collection:

Salivary stones:

Kidney stones: PCHA kidney stones (N=6) were extracted from different patients undergoing either laser lithotripsy, using a holmium laser ureteroscopy basket surgery, or percutaneous nephrolithotomy, in accord with the UCSF Committee on Human Research Protection Program, IRB # 14-14533. All patients provided written informed consent for the collection of specimens to be used for research purposes. No identifiable images were taken and all elements of the research protocol, relevant guidelines, and regulations were strictly adhered to during the course of the study. Kidney PCHA stones were collected from patients who were healthy, other than kidney calcification related diseases (cystinuria, history of kidney stones, renal tubular acidosis, pyelonephritis, urethral stricture and bilateral medullary nephrocalcinosis).

Prostate stones:

High resolution micro-x-ray computed tomography (MXCT): Each set of stones were scanned using high resolution MXCT (Micro-XCT-200, Carl Zeiss Microscopy, Pleasanton, California). Samples were secured in custom holders and scanned using MXCT, under ex-vivo, dry

conditions. MXCT scans were acquired at 4x (5 μm^3/voxel) with 1200 slices per each volumetric reconstruction. The digitally reconstructed micro-XCT was analyzed using AVIZO software 9.0.1 (FEI, Hillsboro, Oregon).

Sample preparation and secondary optical analysis:

Light microscopy: Dehydrated samples were imaged at magnifications between 1x and 4x to fit samples to the field of view of the Olympus SZ61 (Olympus, Shinjuku, Japan).

Specimen preparation: Stones were identified for cutting (Buehler IsoMet low speed saw, Lake Bluff, Illinois) along the stone's shortest cross-sectional axis. Stones were embedded in 4 parts Epoxy Resin (EpoxiCure 2) and 1 part Epoxy Hardener (EpoxiCure 2), polished with graded abrasive paper and micro-cloths from 1200 grit to 0.25 μm, and dehydrated using a graded ethanol and deionized water dilution (50% to 100%).

Autofluorescent microscopy (AF): AF maps were generated at a magnification of 20x, on the Zeiss Axio microscope using the Zeiss Axiocam 506 mono detector (Carl Zeiss, Pleasanton, CA). These maps were collected in red fluorescence (AF568), green fluorescence (AF488), and blue fluorescence (AF405).

Scanning electron microscopy (SEM) and backscattered electron microscopy (BSEM): Samples were mounted to aluminum SEM stage plates with carbon tape, and carbon paint (Ted Pella, Redding, Ca) was distributed along the curved edge of the cylindrical epoxy embedded samples. SEM data was acquired using the Zeiss Gemini Sigma 500 VP (Carl Zeiss, Pleasanton, CA). Low magnification SEM maps of each stone at a magnification of 100x and an energy of 1 KV, shows

topological and large-scale structural features of the stones. High magnification (1,000x-50,000x) SEM images from regions of interest were analyzed and localized within the aforementioned SEM maps. BSE was used to generate atomic mass maps of the samples at a magnification of 100x acquired with the Zeiss Gemini Sigma 500 VP (Carl Zeiss, Pleasanton, CA), at 10 KV of energy.

X-ray fluorescence spectroscopy (XRF) and laser ablative inductively coupled plasma (LA-ICP): XRF data was taken from the Advanced Light Source (ALS) beamline (LBNL, Berkeley, CA) 10.3.2 which provides soft x-rays at an energy of 10 KeV. This XRF data consists of mapping elemental analysis with a spot size of 4μm-10μm, as well as a histogram of ejected photons which was used to identify elements and possible overlap in emission spectra. Using LA-ICP we were able to correlate locations with XRF and BSE data to confirm that the epoxy resin is not having an impact on elemental analysis and as a method to dual-confirm XRF readings. Both XRF and ICP methods collected Zn, Ca, P, Cl, and F at Kα, Kβ, Lα or Lβ emission spectra.

Confocal fluorescence microscopy: Autofluorescence of the stones was measured using a Leica TCS SP5 II inverted confocal laser scanning microscope. After embedding and cutting the samples, the specimens were placed on a thin sample cover (Fisher Premium Coverglass) and irradiated with 405 nm diode light. Fluorescence was measured in the range of 410-480 nm. Samples were scanned with a 20x objective (0.4 NA) and a speed of 200 Hz in bidirectional mode. The pinholes were adjusted to attain an optical thickness of 2 AU. After focusing, the beam intensity was adjusted so that the photomultiplier (PMT) voltage was around 700-800 V and the dynamic range of the detector was used fully. The necessary number of snaps were taken to cover the whole specimen section with a 10% overlap and a resolution of 1024x1024 px. Stitching was carried out by Leica software LAS AF.

CNP size distribution: In this work, we propose an alternative method to estimate the sizes of the CNPs from images of a kidney stone section. The idea is based on the observation that, while well-defined boundaries of individual CNPs may be difficult to identify within a given area, parts of the CNP boundaries are still visible using electrons backscattered by the sample in FE-SEM. Thus, after acquiring the images, we used an edge detection function to estimate the visible perimeter of CNPs within a given box, see Figure 4b. Since the CNPs are relatively spherical and uniform in size within one box, it is possible to derive an effective CNP radius knowing the total edge perimeter and particle area. In particular, the total area and perimeter for a collection of N circular particles are given by: from which an average particle radius can be estimated where N_b represents the total number of black pixels in the box, and N_w represents the number of white pixels after the edge detection transformation. The box can then be moved throughout the image as a moving average to generate an estimated size distribution. A scaling value of k = 2.0 was introduced empirically to improve the agreement between the distributions and the images inspected. To avoid artificially inflating the estimated perimeter, we used the Canny Edge Detector plugin for ImageJ, which generates edges 1 pixel wide. Typical settings for the detector are Gaussian kernel radius of 2.2, low threshold of 2.2, and high threshold of 6.9.

Statistical methods: MXCT data was converted to mineral density and the data's histogram was plotted. This data was then thresholded within 300-3,000 mg/cc and binned 100 times using AVIZO software 9.0.1 (FEI, Hillsboro, Oregon). Histograms were normalized and fit using gaussian curve fitting functions within MATLAB (R2013b, MathWorks Inc., Natick, MA) software package. We checked to ensure that the R^2 value was greater than .95, RMSE was as low as possible and ensured that gaussian fits were visually within reason representative of the data.

Figure 1

Salivary

~~Place holder~~

Kidney

Prostate

a)

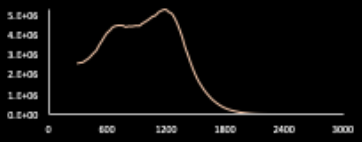

Whole stone MD histogram and bar graph completed

b)

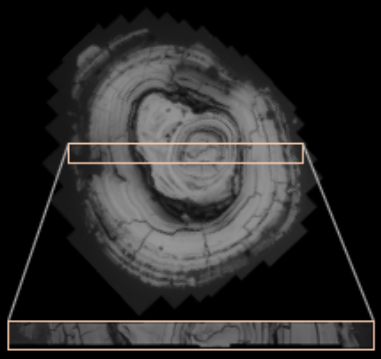

BSE stitch of cross-section

c)

BSE line stitch of cross-section

d)

MD line stitch histogram

e)

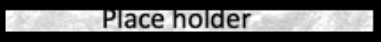

Line stitch Edges

f)

Line stitch MD moving average

g)

Line stitch SMNP radii moving average

h)

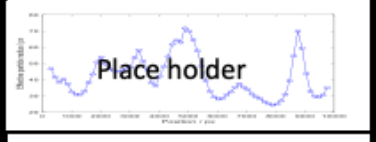

Line stitch Zinc moving average

i)

Line stitch Blue AF moving average

j)

Line stitch Phosphorous moving average

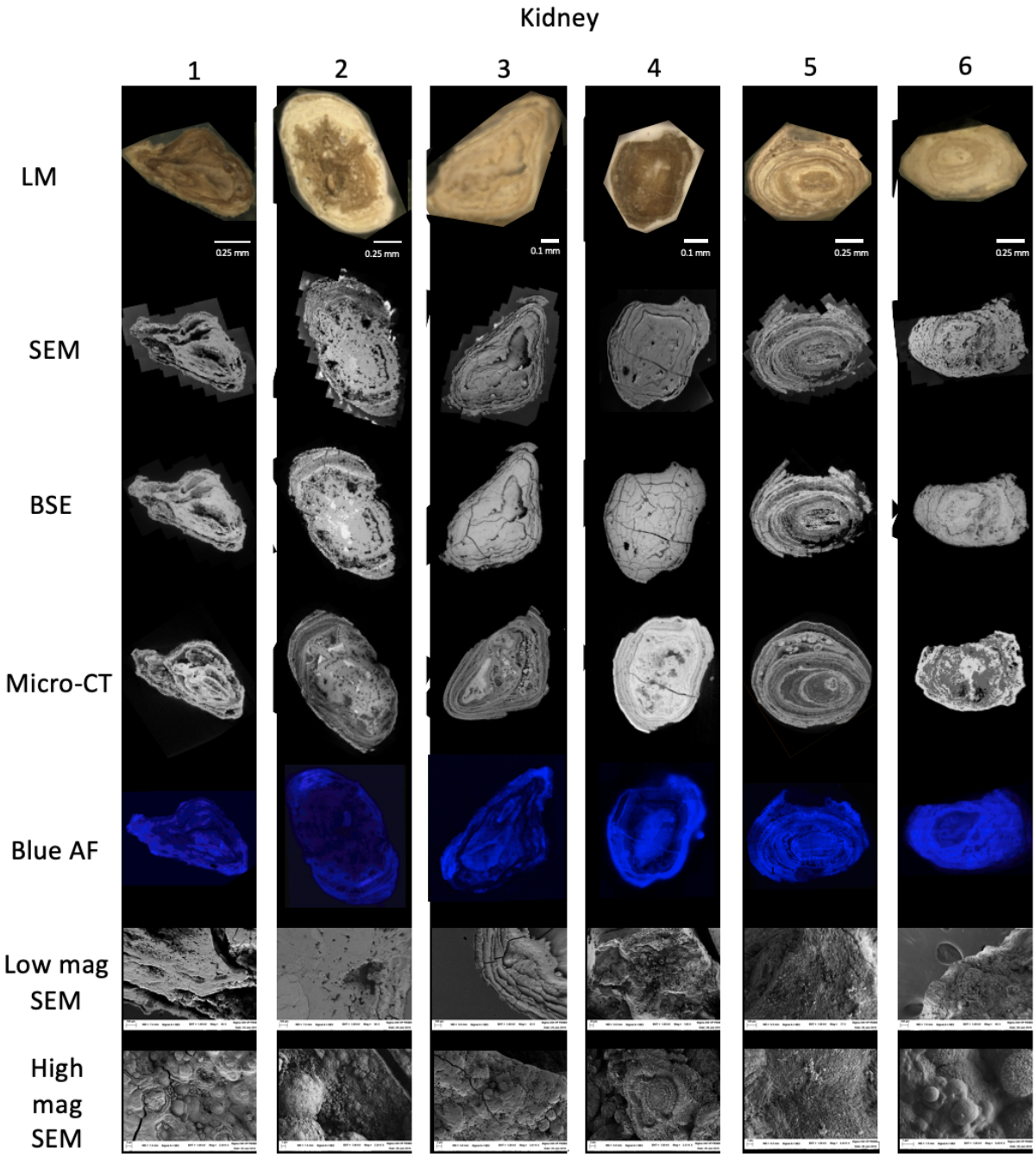
Kidney
1
2
3
4
5
6
LM
SEM
BSE
Micro-CT
Blue AF
Low mag SEM
High mag SEM
0.25 mm
0.25 mm
0.1 mm
0.1 mm
0.25 mm
0.25 mm

Figure 5

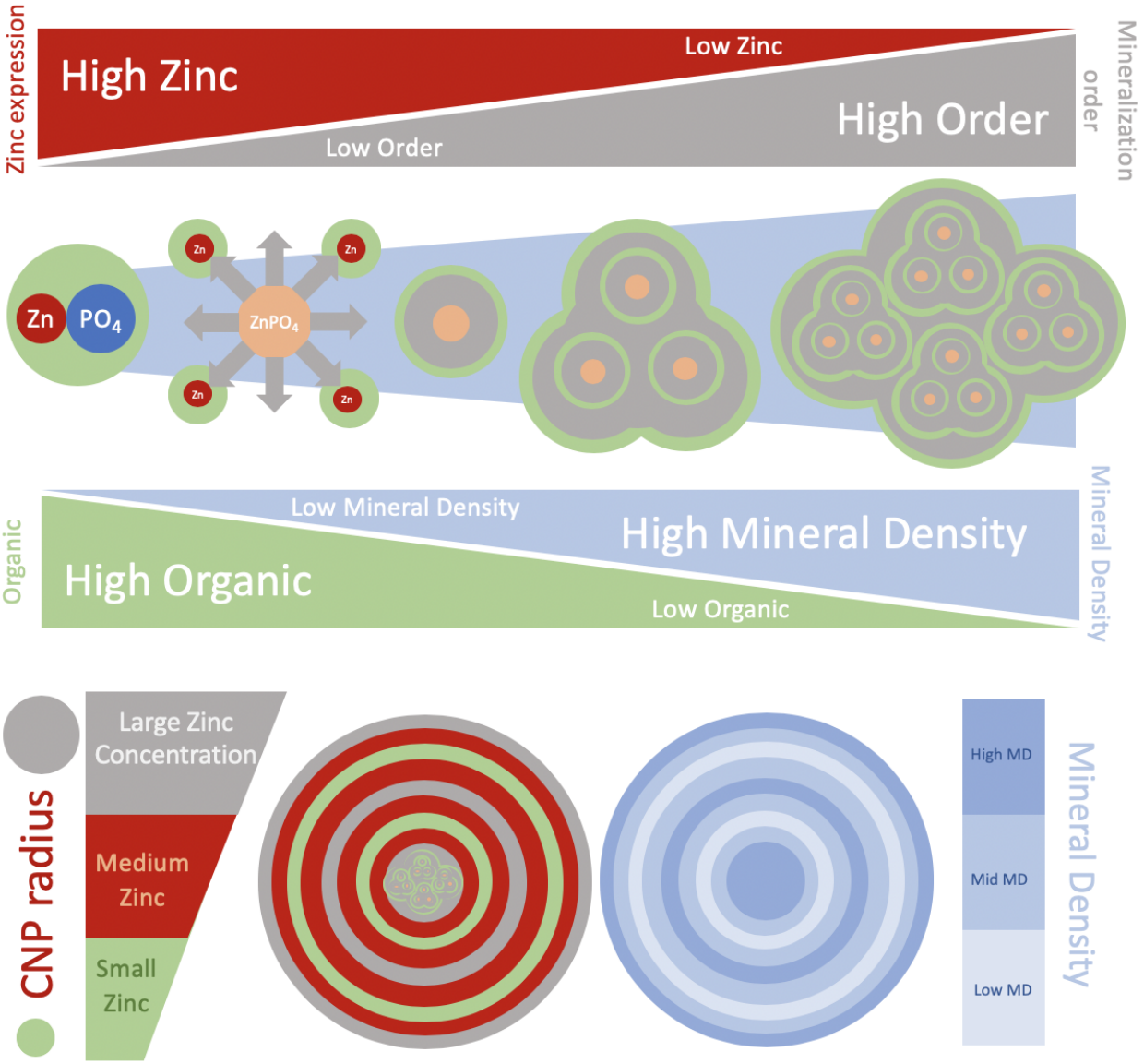
Zinc expression
High Zinc
Low Zinc
Low Order
High Order
Mineralization order
Zn
PO4
ZnPO4
Organic
Low Mineral Density
High Mineral Density
High Organic
Low Organic
Mineral Density
CNP radius
Large Zinc Concentration
Medium Zinc
Small Zinc
High MD
Mid MD
Low MD
Mineral Density

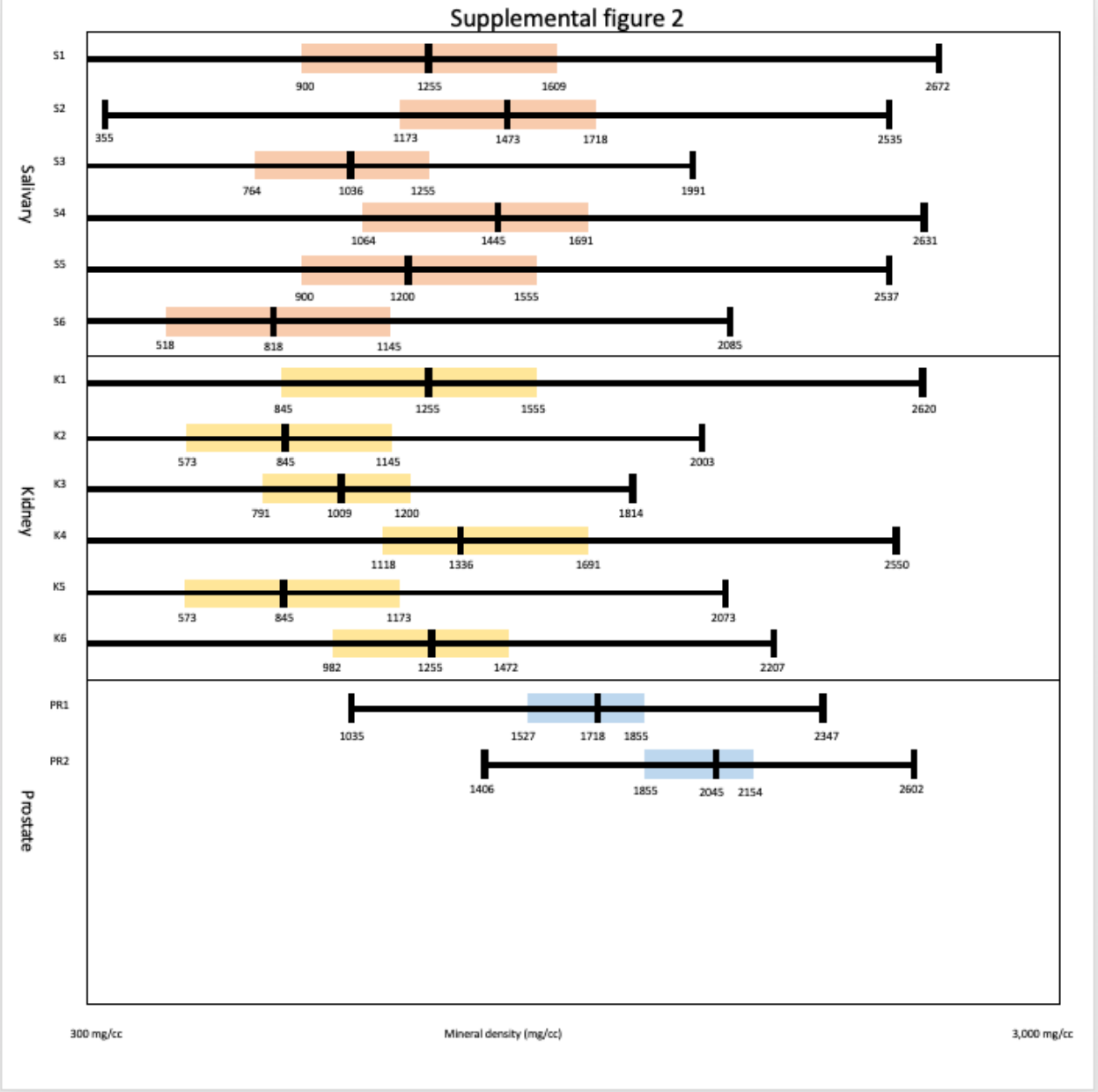

Bibliography

1. Alexander, M. *Biodegradation and bioremediation*. (Academic Press, 1999).
2. Anbu, P., Kang, C. H., Shin, Y. J. & So, J. S. Formations of calcium carbonate minerals by bacteria and its multiple applications. *SpringerPlus* **5**, 1–26 (2016).

3. Min, K. H., Lee, H. J., Lee, S. C. & Park, K. Biomineralized hybrid nanoparticles for imaging and therapy of cancers. *Quantitative Imaging in Medicine and Surgery* **8**, 694–708 (2018).
4. Types of Kidney Stones | UW Health | Madison, WI. Available at: https://www.uwhealth.org/urology/types-of-kidney-stones/11206. (Accessed: 5th December 2019)
5. Definition & Facts for Kidney Stones | NIDDK. Available at: https://www.niddk.nih.gov/health-information/urologic-diseases/kidney-stones/definition-facts. (Accessed: 5th December 2019)
6. KIDNEY STONE TYPES | Kidney Stone Evaluation And Treatment Program. Available at: https://kidneystones.uchicago.edu/kidney-stone-types/. (Accessed: 5th December 2019)
7. Usai, D. *et al.* Late Pleistocene/Early Holocene Evidence of Prostatic Stones at Al Khiday Cemetery, Central Sudan. *PLoS One* **12**, e0169524 (2017).
8. ÇiftÇioğlu, N. & McKay, D. S. Pathological calcification and replicating calcifying-nanoparticles: General approach and correlation. *Pediatric Research* **67**, 490–499 (2010).
9. Johnsson, M. S. A. & Nancollas, G. H. The role of Brushite and octacalcium phosphate in apatite formation. *Critical Reviews in Oral Biology and Medicine* **3**, 61–82 (1992).
10. Kraaij, S., Karagozoglu, K. H., Forouzanfar, T., Veerman, E. C. I. & Brand, H. S. Salivary stones: Symptoms, aetiology, biochemical composition and treatment. *Br. Dent. J.* **217**, E23 (2014).
11. Yao, J. H., Elder, K. R., Guo, H. & Grant, M. Theory and simulation of Ostwald ripening. *Phys. Rev. B* **47**, 14110–14125 (1993).

12. Morta, S., Mante, K., Rasa, B. & Gintaras, J. The influence of salivary pH and calcium/phosphate ions concentration on salivary gland stones' formation. *J. Int. Med. Dent.* **5**, 30–38 (2018).

13. Kraaij, S., Brand, H. S., van der Meij, E. H. & de Visscher, J. G. Biochemical composition of salivary stones in relation to stone-and patient-related factors. *Med. Oral Patol. Oral y Cir. Bucal* **23**, e540–e544 (2018).

14. Yamaguchi, M. Role of nutritional zinc in the prevention of osteoporosis. *Mol. Cell. Biochem.* **338**, 241–254 (2010).

15. HAUMONT, S. DISTRIBUTION OF ZINC IN BONE TISSUE. *J. Histochem. Cytochem.* **9**, 141–145 (1961).

16. Herzberg, M., Foldes, J., Steinberg, R. & Menczel, J. Zinc excretion in osteoporotic women. *J. Bone Miner. Res.* **5**, 251–257 (1990).